UCRL- 98810
PREPRINT

Theoretical Modeling of Czochralski Crystal Growth

Jeffrey J. Derby

This paper was prepared for submittal to
Materials Research Society Bulletin

May 23, 1988

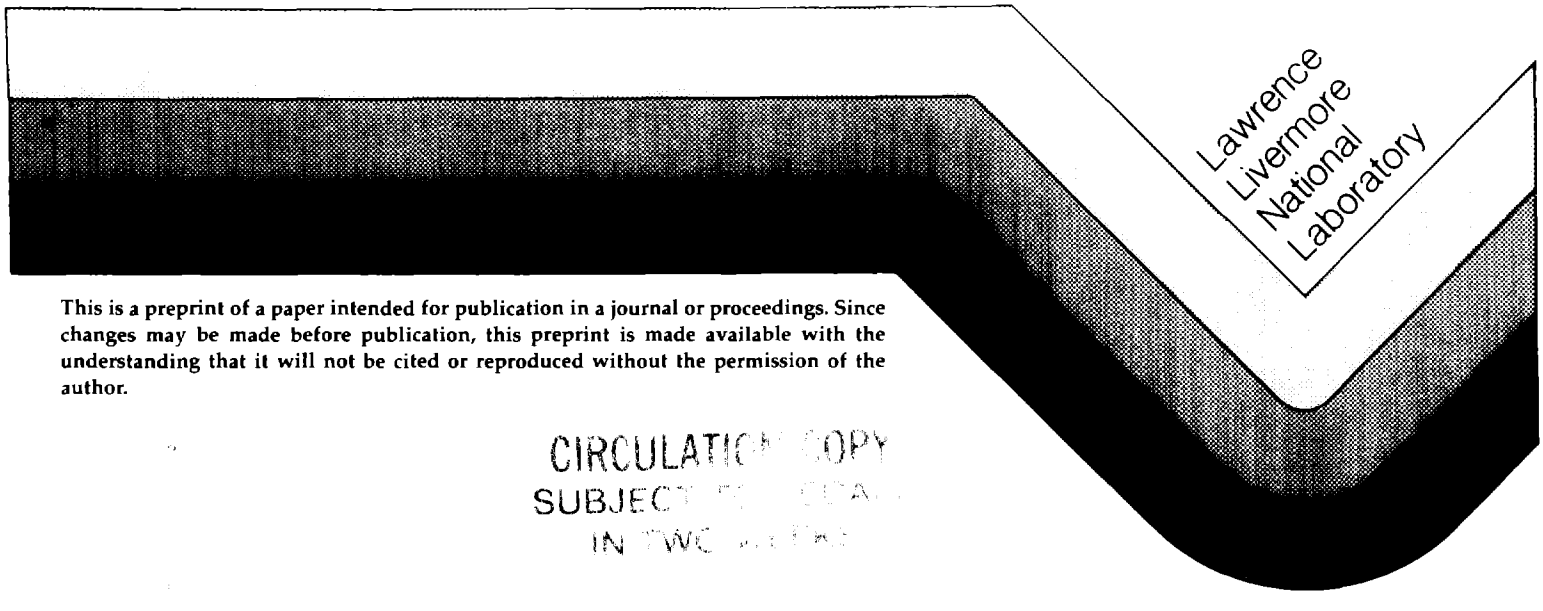

Theoretical Modeling of Czochralski Crystal Growth

Jeffrey J. Derby

Lawrence Livermore National Laboratory
University of California
Livermore, CA 94550

Introduction

The growth of single crystals with precisely-controlled properties is one of the most demanding goals of modern materials processing, and its realization depends on the application of fundamentals from solid-state physics, chemistry, thermodynamics, and transport phenomena. Bulk semiconductor substrates and many high-power solid-state laser host materials are typically produced by solidification from the melt. The quality of the crystals produced in this manner hinges on process conditions which are predominantly determined by the transport of heat, mass, and momentum in the melt and crystal. Accurate modeling of melt crystal growth promises to enhance our understanding of existing systems and improve the design and control of future processes, thereby accelerating the development of advanced materials and devices.

Theoretical modeling often is the only way to probe the complex interactions which characterize melt crystal growth, especially the effects of process changes on internal features of growth which cannot be directly measured on-line, such as the shape of the melt/crystal interface or temperature gradients within the growing crystal. In this way, computer simulation can serve as a design tool for developing control strategies and process innovations. Further, modeling serves as a test bed for theoretical experiments which extend our knowledge of how fundamental physical phenomena govern the process.

This report attempts to provide a glimpse of how analysis and modeling have impacted the understanding of Czochralski (CZ) crystal growth. The reader is referred to several excellent reviews [1-3] for

more in-depth information regarding melt crystal growth modeling. In the following sections, the physical transport mechanisms of CZ growth are analyzed, sample results are presented for semiconductor and oxide growth simulations, an assessment of the current state of the art of modeling is discussed, and future developments are projected.

Analysis

Often the successful practice of crystal growth relies on experiential intuition; however, the underlying science of crystal growth is based on the strong foundation of first principles. Our goal is to obtain a fundamental understanding of the controlling features of CZ growth by assessing the underlying physical phenomena. These features can vary widely for different materials and processes, leading to the dilemma in analyzing crystal growth systems that few theoretical generalizations are both practically useful and universally valid. In spite of this difficulty, two typical systems are appraised which are representative of the major materials produced by the Czochralski method, a semiconductor, silicon, and an oxide, gadolinium gallium garnet ($Gd_3Ga_5O_{12}$, hereafter referred to as GGG).

The Czochralski method is illustrated schematically in Fig. 1a for a typical oxide growth process. A single-crystal seed is dipped into a crucible filled with molten material, allowed to equilibrate, and slowly withdrawn upward. Upon the successful initiation of growth from the seed, suitable manipulations of the process parameters, such as pull rate and heater power, prompt the crystal to grow out and maintain a constant diameter as the melt is depleted from the crucible. At the end of the growth run, the crystal is slowly cooled to ambient temperature and is then removed for subsequent device processing.

A typical semiconductor CZ growth system is very similar to that depicted in Fig. 1a, but the crucible is often heated by a surrounding resistance heater. The liquid-encapsulated Czochralski (LEC) method, in which the crystal is grown through a floating layer of inert material designed to contain volatile species in the melt, is an important means of producing compound semiconductors.

Understanding Czochralski crystal growth involves analysis on several disparate length and time scales. Characteristic scales are listed in Table 1, and three length scales used to classify the CZ process are shown schematically in Fig. 1. The macro-scale comprises the entire growth station, the intermediate scale includes the crystal and melt, and the micro-scale embodies phenomena occurring at phase boundaries. Ultimately, the quality of the crystal is expressed in micro-scale quantities such as concentration distribution, stress distribution, and dislocations. However, attempts to influence the process necessarily occur at the macro-scale. The coupling of widely different physical phenomena at each level is the primary challenge of theoretical analysis and is where the test-bed of modeling can have the most impact on improving a given process, as compared with the Edisonian approach of experimental trial and error. This analysis focuses primarily on the intermediate scale as a continuum, similar to the approach highlighted in [4], and connections with the macro- and micro-scales are accomplished through the appropriate application of boundary conditions and constitutive relations.

The flow of the melt is driven by the temperature field through buoyancy forces and surface tension forces, by crystal and crucible rotation, and by the solidification of melt to crystal. Intense buoyancy-driven flows are a prevailing feature of melt growth. The importance of this mechanism is estimated by the Grashof number, Gr, defined in Table 2. For CZ silicon and GGG growth, the Grashof number is very large, and a free-fall velocity associated with buoyancy-driven flows is approximately 1-10 cm/s, see Table 1. Flows caused by temperature induced surface-tension gradients can also be intense for these systems, as indicated by Marangoni numbers, Ma, which are significant. If thermocapillary flows dominate and surface-tension effects balance viscous forces in a boundary layer at the meniscus [5], the characteristic velocity for both systems is estimated to be as high as 1-10 cm/s. Flows caused by solidification are nearly equivalent to the crystal pull rate and are several orders of magnitude lower than those driven by buoyancy or surface tension gradients.

Additional driving forces for flow are crystal and crucible rotation, leading to characteristic velocities as large as 10 cm/s. The flows impressed on the system by rotation can be as large as those which naturally arise; however, these flows are directed azimuthally and impact the meridional natural convective flows in a secondary manner. The complexities of rotational flows and their interactions with buoyancy-driven flows will not be addressed, see [6,7] for further discussions of flows of this type.

The celebrated Reynolds number, Re, can be thought of as a ratio between inertial forces and viscous forces. When this number is large, the flow is dominated by nonlinear convective terms, complicating both the physics and the methodology for solution of the governing equations. Using estimates of the maximum characteristic velocities of Table 1, the estimated Reynolds number is large, $Re>10^3$ for both systems, indicating that inertial forces are important and that momentum boundary layers are likely to form along the bounding surfaces of the melt. When intense buoyancy flows dominate the flow field, the Reynolds number scales with the square root of the Grashof number, $Re \sim Gr^{1/2}$.

The application of a strong magnetic field to semiconductor systems can effectively damp meridional flow in the melt [8], and this technique is actively being explored for controlling heat and mass transfer in CZ growth. For oxide systems and for semiconductor growth in the absence of magnetic stabilization, the direct control of buoyancy-driven and Marangoni flow is nearly impossible. The driving forces for flow can be reduced by decreasing length scales and temperature gradients across the melt, but this is often at the expense of conditions needed to maintain the growth of the crystal. Crystal and crucible rotation can also influence the flow state, but as alluded to previously, the interaction of rotational and meridional flow is extremely complex. Crystal rotation has been used effectively to modify the flow field adjacent to the solidification interface. A detailed discussion of hydrodynamics in crystal growth systems is given by Carruthers [6].

The ratios of hydrodynamic and surface tension normal forces at the meniscus are expressed in terms of the Bond number, Weber number, and Capillary number, defined in Table 2. The Bond number is a ratio of gravity-induced hydrostatic pressure and surface tension forces. The relatively large Bond numbers for both systems indicate that gravity forces will level most of the melt free surface; however, curvature will occur near the tri-junction of melt, crystal, and ambient, over a characteristic length scale of less than a centimeter (see Table 1). Since the surface tension of these melts is quite high, fluid mechanical forces do not play a large role in setting the meniscus shape. When the dynamic pressure field is sufficiently modified, such as during fast crucible or crystal rotation, the Weber number can become large enough to affect the shape of the free surface. On the other hand, viscous forces acting on the interface are invariably negligible, as evidenced by the very small Capillary numbers for the two systems.

An appropriate energy balance includes transport via conduction, convection, and radiation by transmission through the medium. The importance of heat transfer by convection to that by pure conduction is represented by the dimensionless Peclet number for heat transfer, Pe. The Peclet number is the product of the Reynolds number and the Prandtl number, Pr, which is a material constant representing the ratio of momentum diffusion to heat diffusion. The effect of fluid flow on heat transfer increases for materials with larger Prandtl numbers, and vice versa. The Prandtl number for molten semiconductors is approximately 10^{-2}, while it is believed to be from 1-10 for oxide melts. For

flows of comparable intensity, heat transfer by convection is much more important in an oxide growth system than in a semiconductor melt. However, as indicated by the estimates in Table 2, convective heat transfer plays an important role in both semiconductor and oxide systems; this is demonstrated by calculations in [9]. In semiconductor systems, convective heat transfer in the melt can be suppressed by magnetic stabilization of the flow field, as discussed previously.

The flow of radiative energy through a medium occurs when temperatures are sufficiently high and the medium is sufficiently transparent to black-body thermal radiation at those temperatures. The importance of internal radiation heat transfer is estimated by computing the ratio of conductive flux to radiative flux. For an optically thick medium ($a_R L >> 1$, where a_R is the spectral absorbance and L is a characteristic length), this ratio is approximated by the conduction-to-radiation parameter N [10] in Table 2. Internal radiative heat transport is probably minor in silicon systems but may be quite important for GGG growth. This coarse estimate tends to exaggerate the importance of radiative transport for systems which are not optically thick, yet experimental evidence suggests that internal radiative transfer may be important in the growth of other oxide crystals, such as YAG, yttrium aluminum garnet [11]. In this case, optically active dopants and radiative exchange features of the furnace, such as heat shields near the crystal, can be expected to have a large impact on growth conditions.

Solidification at the melt/crystal interface releases latent heat to the surroundings. The importance of this heat source on modifying the local temperature field is estimated by the product of the solid phase Peclet number, Pe_s, and the Stefan number, S, referred to as the modified Stefan number in Table 2. The magnitude of these quantities indicate that latent heat is significant in semiconductor growth but much less so in oxide growth. Consequently, the pull rate of the crystal will have an important effect on heat transfer only in semiconductor systems.

Exterior surfaces communicate with the furnace enclosure by two mechanisms, convective cooling into the gaseous ambient and radiation energy exchange with enclosure surfaces. The Biot and Radiation numbers are measures of the relative importance of these mechanisms. For both systems, radiation heat transfer is predominant and severely complicates the thermal environment within a conventional CZ puller. Since radiative heat transfer is an inherently nonlinear phenomenon characterized by long-range interactions, subtle changes in enclosure geometry can have profound effects on heat transfer.

A species in a fluid is transported by convection and molecular diffusion. The importance of these different modes of mass transfer can be assessed in a manner similar to the analysis for heat transfer presented above. The importance of fluid flow on the transport of a dilute dopant in the melt is represented by the solutal Peclet number, Pe_C=ReSc, where Sc is the Schmidt number, the mass transfer analog of the Prandtl number. Using values for V and L listed in Table 1 and estimating a binary diffusion coefficient of $D_{AB} = 10^{-5}$-10^{-4} cm^2/s,

the solutal Peclet number is very large, $Pe_c = 10^5$-10^7, hence convection plays the primary role in setting mass transfer in melt crystal growth. Convective mass transfer will remain dominant in magnetic CZ semiconductor melts long after convective heat transfer has been suppressed, since the Schmidt number is so much larger than the Prandtl number.

The extreme sensitivity of mass transfer to convection places added import on the need to accurately predict fluid flow in these systems. This sensitivity also situates these problems among the most difficult numerical simulations of today. A sense of some of the obstacles encountered in these calculations can be inferred from the characteristic length scales in Table 1. Solute transport into the crystal is controlled by phenomena occurring in a boundary layer which is as much as three orders of magnitude smaller than the dimensions of the melt, and within this thin boundary layer adjacent to the melt/crystal interface, both the effects of bulk hydrodynamics and flow due to solidification are important [1].

Modeling

Czochralski growth analysis dates back over thirty years to the period when the CZ method was first being applied to the growth of semiconductor crystals. Billig [12] derived an analytical relation to describe the effect of pull rate on the radius of a germanium crystal. With the advent of high-speed digital computers, numerical modeling of heat transfer and fluid flow elucidated many features of bulk melt

behavior [3,13]. However, none of these efforts have been able to investigate the coupling of interfacial phenomena and field quantities which is crucial for understanding how process conditions ultimately affect the crystal end-product.

Thermal-capillary models presented by Crowley [14] and Derby et al. [15] were the first efforts to comprehensively describe the interaction of heat transfer with interfacial phenomena in semiconductor systems. Unfortunately, these analysis are only valid where the characteristic velocity in the melt is small, so that conduction is dominant and $Pe << 1$. Recently, Derby et al. [16] have extended their model to include system dynamics and moving interfaces, and Sackinger et al. [9] have incorporated axisymmetric, steady-state fluid mechanics to the thermal-capillary model. Here, we present sample results from these models and explore the strengths and weaknesses of such approaches.

The model domains comprise regions of melt, crystal, and crucible; an encapsulant layer is included for the simulation of liquid-encapsulated Czochralski growth of gallium arsenide (see Fig. 2a) and pedestal and crucible insulation are included for the GGG simulation (see Fig. 5a). The model LEC crucible is radiatively heated by a resistance heater at constant temperature, whereas heat is deposited directly into the crucible via induction heating in the GGG system. Cooling of the model surfaces is calculated by Gebhart's method for a diffuse-grey enclosure so that the detailed exchange of radiation is captured. These two pathways for heat flow into and out of the system serve to link the intermediate scale with the surrounding macro-scale (see Fig. 1).

The melt/crystal interface is placed along the melting point isotherm of the system. The meniscus is determined by a normal force balance which accounts for capillarity, gravity forces, and hydrodynamic effects. The shape of the crystal evolves from an overall balance of heat transfer coupled with a detailed description of wetting angles at the melt/crystal/ambient tri-junction. These features connect the continuum model with the micro-scale phenomena of crystal growth.

The equations which describe the process are discretized by the Galerkin finite element method over an adaptive mesh of quadrilateral elements. The mesh deforms to follow the positions of the melt/crystal interface, the melt meniscus (and encapsulant meniscus for LEC growth), and the shape of the crystal. Nonlinearities are present in the equation set from radiation heat transfer and melt hydrodynamics, and the free-boundaries introduce additional strong nonlinearities. Consequently, a sophisticated quasi-Newton iteration scheme is employed to efficiently solve the model equations.

LEC Gallium Arsenide Growth

Brown and colleagues [15-17] at the Massachusetts Institute of Technology have developed a fully dynamic, thermal-capillary model for conduction-dominated systems which, although inappropriate for moderate to large-scale semiconductor systems (where the Peclet number in the melt is significant, see Table 2), is valid for semiconductor systems when a strong magnetic field is applied to damp convection. Results are presented here from the study of Thomas et al. [17] for the theoretical simulation of an experimental LEC growth run.

The experiment was performed using a Hamco model 3000 crystal puller modified for LEC growth of gallium arsenide by M.J. Wargo and A.F. Witt of the Department of Materials Science and Engineering at the Massachusetts Institute of Technology. The six inch diameter crucible was heated by a graphite resistance heater, and the growth took place with an applied axial magnetic field of 4,000 gauss, enough to completely damp convective heat transfer through the melt. The heater temperature set point and pull rate history were directly input to the dynamic thermal-capillary model to simulate growth conditions.

Figure 2 details the evolution of the model predictions; the system interfaces are shown with temperature contours plotted at 25 K increments about the melting point temperature of gallium arsenide (1511 K). The initial configuration for the simulation is the steady-state solution shown in Fig. 2a. Heat flows through the system from the heated crucible outer wall, downward to the crucible base and upward to the encapsulant and crystal surfaces. The seed crystal displays a nearly one-dimensional temperature distribution, although some radiative heating of the seed just above the encapsulant surface is visible.

A drop in heater power causes the crystal to grow initially outward from the seed. The cone of the crystal after four hours of growth is clearly seen in Fig. 2b. As more of the crystal emerges from the encapsulant and views the hot crucible wall, cooling is inhibited, and the crystal radius tends to decrease. This trend accelerates as the inward sloping crystal face views the hot encapsulant and melt surfaces

below. Apparent at all times is the drastic change in the radial temperature gradient of the crystal as it exits the encapsulant. This effect very likely produces large thermal stresses which can abet the formation of dislocations in the crystal.

The final theoretical crystal shape is compared with an outline of the actual crystal in Figure 3. The theoretical shape captures many of the features of the experimental crystal, although the actual rates of diameter increase and decrease are under-predicted. Nevertheless, the model predictions are within approximately 20 percent of the experiment, a result which is very encouraging considering the inaccuracies in thermophysical properties and model idealizations regarding heat transfer through the boric oxide encapsulant, see [17] for further details.

CZ Oxide Growth

The addition of melt fluid mechanics is a requisite for describing the CZ growth of oxide materials, since convective heat transfer predominates in the melt. This extension to the thermal-capillary model is presented in [9], and a detailed analysis of induction heating of the crucible is given in [18]. The resulting integrated process model is described in [19], and sample results from that analysis are shown here.

The CZ method is a transient batch process, since the crucible slowly empties with time. However, we invoke a quasi-steady-state assumption to describe transport phenomena and interface shapes in the system, depicting the growth process by calculations with the melt volume as a parameter and each simulation as a snapshot in time. This assumption is

warranted by the disparate time scales which characterize the process, see Table 1. Compared with process times of several days or longer, all other phenomena occur on a vanishingly small time scale.

The time-averaged power distribution delivered to an eight inch diameter iridium crucible by the induction heating system is shown in Fig. 4. This distribution is used as input for the GGG growth simulations shown in Fig. 5, where each calculation employs a steady-state controller which adjusts the absolute level of power to the crucible in order to achieve a crystal of desired radius. Isotherms spaced at 40K about the melting point (2023 K) are shown on the left side of the figure, and streamlines are displayed on the right half of the plot. In these calculations, crystal and crucible rotation and thermocapillary flow are not included; only steady, axisymmetric, buoyancy-driven flow is considered.

A nearly linear axial temperature distribution is present in the crystal in Fig. 5a, and the influence of radiative heat transfer into the crystal from the hot crucible wall is evident at the crystal surface by the upward deflection of the temperature contours. Large gradients through the pedestal and insulation result from the low conductivity of these regions and the large temperature drop across them. The temperature field in the melt exhibits a well-mixed, nearly isothermal core with boundary layers, and the melt/crystal interface is deflected toward the melt by the convective effects of the flow turning downward at the centerline.

The streamlines show a primary recirculation cell driven by buoyancy; warm fluid rises along the crucible wall and cooler fluid falls at the centerline. A secondary vortex nested within the primary vortex is

apparent near the bottom center of the crucible along with a small counter-rotating vortex attached to the bottom of the crucible. This structure results from the stratified density distribution along the bottom of the crucible. Since the bottom of the crucible is losing heat to the pedestal, there is a region of cooler liquid underlying warmer, lighter fluid. As the flow down the centerline plunges through this density gradient, an opposing force is experienced which gives rise to the vortex pattern. This phenomenon is often observed in the lee of a mountain range when warm air descends into a valley of stably-stratified cool air.

Another less apparent flow feature is the vortex spanning the upper corner of the domain, from wall to meniscus. Similar separation arises in low Prandtl number fluids near the appearance of time-dependent flows [20], and this feature may also signal a pluming instability caused by the destabilizing axial temperature gradient at the surface of the melt. This computed steady flow state may very well be physically unstable; however, calculations to confirm this hypothesis have not yet been performed.

As the melt level drops, the crystal views more of the hot crucible wall, decreasing the overall cooling of the crystal. Even though a constant radius has been maintained, the axial temperature gradients in the crystal have decreased enormously. The structure and intensity of the flow also change as the melt level drops, with the maximum velocity decreasing as temperature gradients decrease and as the melt aspect ratio becomes progressively flatter. The effects of heat loss from the bottom of the crucible are still discernible by the melt isotherms and the wavy streamlines in Fig. 5c.

Initially the power to the crucible decreases slowly with depletion of the melt, from 36.9 KW in Fig. 5a to 36.8 KW in Fig. 5b, and at the end of the run the power level rises slightly to 37.2 KW. As the crystal grows deeper into the crucible, wall radiation reduces the cooling of the crystal, thereby decreasing the needed power to maintain a constant radius. Simultaneously, convective heat flow through the melt diminishes since the characteristic velocity is decreasing, and this tends to increase the needed power to the crucible. These competing heat transfer mechanisms tend to counterbalance, so that in spite of significant changes in melt geometry, power changes are nearly constant over much of the run. This indicates that diameter control in oxide growth is less demanding than one might expect from the inherent complexity of the process.

Summary

Dramatic advances in modeling sophistication over the past decade has rendered simulations capable of capturing realistic complexity in melt crystal growth. The physical understanding achieved through such modeling in itself is notable, since clearer understanding will enable process advances. The use of models as more expedient and cost-effective alternatives to laboratory experiments for testing new ideas and concepts is becoming feasible.

However, in spite of the tremendous gains, several hurdles remain. The complexity of real-life hydrodynamics cannot be underestimated in melt crystal growth. In low Prandtl number semiconductor systems, flows are most likely time-dependent or chaotic for all but the smallest

systems unless a strong magnetic field is applied. Similar complexity also exists for large-scale oxide systems, although the mechanisms of flow instability are inherently different. Rotational flows interacting with buoyancy flows are also notoriously complex, often three-dimensional and time-dependent.

Without accurate knowledge of fluid mechanics, we cannot hope to accurately perform mass transfer calculations for dopants in these systems. As discussed previously, convection-dominated mass transfer and transport through boundary layers pose some of the most difficult of numerical problems. Indeed, this is a premier area of research in computational methods today.

Heat transport calculation poses other problems, mostly with regard to radiative transfer. As discussed above, heat transport via internal radiation may be very important for some systems, notably oxides. The integro-differential equations which describe coupled conduction and radiation have been solved only for a few idealized systems.

More research is needed on constitutive relations or other methods to bridge the disparate length scales which characterize microscopic phenomena and macroscopic field quantities [1,2,4]. The assumption that the melt/crystal interface lies along the melting point isotherm does not take into account the crystallographic effects of facetting nor the formation of a cellular interface. The length scale for these phenomena, indicated in Table 1, is up to six orders of magnitude smaller than the macroscopic length scale for the system, making direct coupled calculations infeasible at present and unlikely in the near future. A related issue concerns dislocation creation and propagation in a thermally-induced stress field.

A final impediment is the dearth of thermophysical property measurements for high-temperature semiconductor and oxide systems. Although performing such property measurements is unglamorous and expensive, they must be performed if the full value of modern simulation is to be realized.

What does the future hold and where are we going? Unless dramatic changes occur in computer hardware or numerical algorithms, the daunting prospect of direct three-dimensional time-dependent simulation of a large-scale CZ puller seems unlikely and inappropriate, at least in the near-term future. The most promising area is the use of modeling to redesign systems or map out optimal windows of operation, for example, conditions where melt hydrodynamics can be expected to be axisymmetric and time-independent. The use of strong magnetic fields coupled with theoretical analysis is an excellent example of this approach. Modeling will also directly address the inverse problem of process design and the optimization of control strategies, leading eventually to model-based on-line control. In these specific ways and by enlarging the fundamental knowledge base, modeling will have an increasingly major impact on the practice of crystal growth.

Acknowledgements

The author would like to acknowledge significant contributions from L.J. Atherton, R.A. Brown, P.M. Gresho, P.A. Sackinger, P.D. Thomas, and M.J. Wargo. Treva Mauch assisted in document preparation and clearing bureaucratic hurdles. This work was performed under the auspices of the U.S. Department of Energy by Lawrence Livermore National Laboratory under Contract W-7405-Eng-48.

List of Symbols

a_R	Spectral absorbtion coefficient
C_p	Heat capacity
$\mathcal{D}_{AB}$	Binary diffusion coefficient
g	Gravitational constant
h	Heat transfer coefficient
k	Thermal conductivity
L	Characteristic length, crucible radius
n	Index of refraction
R	Crystal radius
T_R	Characteristic temperature for radiation
V	Characteristic velocity
V_p	Crystal pull rate

Greek Symbols

α_m	Thermal diffusivity in melt
α_s	Thermal diffusivity in crystal
β	Coefficient of thermal expansion
γ	Surface tension
$\frac{d\gamma}{dT}$	Thermocapillary coefficient
ΔH_f	Heat of fusion
ΔT	Characteristic temperature difference
ϵ	Emissivity
λ_0	Wavelength for interface morphology
μ	Viscosity
ν	Kinematic viscosity
ρ	Density
σ	Stefan-Boltzmann constant
ω	Induction heater frequency
Ω_c	Crucible rotation rate
Ω_s	Crystal rotation rate

References

1. R.A. Brown, AIChE J. (1988) in press.

2. M.E. Glicksman, S.R. Coriell, and G.B. McFadden, Ann. Rev. Fluid Mech. **18** (1986) p. 307-335.

3. W.E. Langlois, Ann. Rev. Fluid Mech. **17** (1985) p. 191-215.

4. L. Davison, MRS Bulletin **13** (2) (1988) p. 16-21.

5. R. Balasubramaniam and S. Ostrach, PCH PhysichoChemical Hydrodynamics **5** (1) (1984) p. 3-18.

6. J.R. Carruthers, in Preparation and Properties of Solid State Materials, Vol. 3, edited by W.R. Wilcox and R.A. Lefever (Marcel Dekker, New York, 1977) p. 1-121.

7. H.P. Greenspan, The Theory of Rotating Fluids (Cambridge University Press, London, 1968).

8. D.T.J. Hurle, in Crystal Growth, edited by H.S. Peiser (Pergamon, London, 1967) p. 659; H.P. Utech and M.C. Flemings, ibid., p. 651.

9. P.A. Sackinger, R.A. Brown, and J.J. Derby, Int. J. Numer. Meths. Fluids (1988) submitted.

10. M.N. Ozisik, Radiative Transfer and Interactions with Conduction and Convection (Wiley, New York, 1973).

11. B. Cockayne, M. Chesswas, and D.B. Gasson, J. Mater. Sci. 4 (1969) p. 450-456.

12. E. Billig, Proc. R. Soc. Lond. A 229 (1955) p. 346-363.

13. N. Kobayashi, in Preparation and Properties of Solid State Materials, Vol. 6, edited by W.R. Wilcox (Marcel Dekker, New York, 1981) p. 119-253.

14. A.B. Crowley, IMA J. Appl. Math. 30 (1983) p. 173-189.

15. J.J. Derby, R.A. Brown, F.T. Geyling, A.S. Jordan, and G.A. Nikolakopoulou, J. Electrochem. Soc. 132 (1985) p. 470-482.

16. J.J. Derby, L.J. Atherton, P.D. Thomas, and R.A. Brown, J. Sci. Computing 2 (4) (1987) p. 297-343.

17. P.D. Thomas, J.J. Derby, L.J. Atherton, R.A. Brown, M.J. Wargo, and A.F. Witt, J. Crystal Growth (1988) submitted.

18. P.M. Gresho and J.J. Derby, J. Crystal Growth 85 (1987) p. 40-48.

19. J.J. Derby, L.J. Atherton, and P.M. Gresho, J. Crystal Growth (1988) submitted.

20. A. Bottaro and A. Zebib, Phys. Fluids 31 (3) (1988) p. 495-501.

Characteristic Length Scales (cm)			
Description	Expression	Si	GGG
Crucible Radius	L	10	10
Meniscus curvature	$\sqrt{\gamma/\rho g}$	$10^{-1} - 1$	10^{-1}
Diffusion boundary layer	$\mathcal{D}_{AB}/V_p$	$10^{-2} - 10^{-1}$	$1 - 10$
Concentration boundary layer	$L\,Pe_c^{-1/3}$	$10^{-2} - 10^{-1}$	$10^{-2} - 10^{-1}$
Solidification wavelength	λ_0	$10^{-5} - 10^{-1}$	

Characteristic Time Scales (s)			
Description	Expression	Si	GGG
Geometrical time scale	L/V_p	$10^4 - 10^5$	$10^5 - 10^6$
Conduction time scale	L^2/α_m	10^2	10^3
Convection time scale	L/V	$1 - 10$	$1 - 10$
Induction time scale	ω^{-1}	$10^{-5} - 10^{-4}$	

Characteristic Velocities (cm/s)			
Description	Expression	Si	GGG
Buoyancy-driven flow	$\sqrt{g\beta\Delta T L}$	$1 - 10$	$1 - 10$
Surface tension-driven (Marangoni) flow	$\left[\left(\frac{d\gamma}{dT}\right)^2 \frac{(\Delta T)^2\nu}{\mu^2 L}\right]^{1/3}$	$1 - 10$	$10^{-1} - 1$
Crystal pull velocity	V_p	$10^{-4} - 10^{-3}$	$10^{-6} - 10^{-5}$
Forced convection, crystal	$2\pi R\Omega_s$	$0 - 10$	
Forced convection, crucible	$2\pi L\Omega_c$	$0 - 10$	

Table 1. Order-of-magnitude estimates for characteristic scales of length, time, and velocity for the CZ process.

Fluid Mechanics				
Name	Definition	Description	Si	GGG
Grashof Number	$Gr \equiv \frac{g\beta\Delta T L^3}{\nu^2}$	$\frac{\text{Buoyancy force}}{\text{Viscous force}}$	$10^8 - 10^9$	$10^6 - 10^8$
Marangoni Number	$Ma \equiv \frac{\frac{d\gamma}{dT}\Delta T L}{\mu\nu}$	$\frac{\text{Surface tension gradient}}{\text{Viscous force}}$	$10^6 - 10^7$	$10^2 - 10^3$
Reynolds Number	$Re \equiv \frac{VL}{\nu}$	$\frac{\text{Inertial force}}{\text{Viscous force}}$	$10^4 - 10^5$	$10^3 - 10^4$
Bond Number	$Bo \equiv \frac{g\rho L^2}{\gamma}$	$\frac{\text{Hydrostatic force}}{\text{Surface Tension force}}$	10^2	$10^2 - 10^3$
Weber Number	$We \equiv \frac{\rho V^2 L}{\gamma}$	$\frac{\text{Inertial force}}{\text{Surface tension force}}$	$10^{-2} - 1$	$10^{-2} - 10$
Capillary Number	$Ca \equiv \frac{V\mu}{\gamma}$	$\frac{\text{Viscous force}}{\text{Surface tension force}}$	10^{-4}	$10^{-3} - 10^{-2}$

Heat Transfer				
Name	Definition	Description	Si	GGG
Prandtl Number	$Pr \equiv \frac{\nu}{\alpha_m}$	$\frac{\text{Momentum diffusivity}}{\text{Thermal diffusivity}}$	10^{-2}	$1 - 10$
Peclet Number	$Pe = RePr \equiv \frac{VL}{\alpha_m}$	$\frac{\text{Convective heat transport}}{\text{Conductive heat transport}}$	$10^2 - 10^3$	$10^3 - 10^5$
C-R Parameter	$N \equiv \frac{k a_R}{4n^2\sigma T_R^3}$	$\frac{\text{Conductive flux}}{\text{Radiative flux}} (a_R L \gg 1)$	$1 - 10$	$10^{-1} - 10$
Modified Stefan No.	$Pe_s S \equiv \frac{V_p L \Delta H_f}{\alpha_s C_p \Delta T}$	$\frac{\text{Latent heat release}}{\text{Conductive flux}}$	1	$10^{-2} - 10^{-1}$
Biot Number	$Bi \equiv \frac{hL}{k}$	$\frac{\text{Convective surface flux}}{\text{Conduction to surface}}$	10^{-2}	$10^{-2} - 10^{-1}$
Radiation Number	$Ra \equiv \frac{\epsilon\sigma T_R^3 L}{k}$	$\frac{\text{Radiative surface flux}}{\text{Conduction to surface}}$	1	$1 - 10$

Mass Transfer				
Name	Definition	Description	Si	GGG
Schmidt Number	$Sc \equiv \frac{\nu}{\mathcal{D}_{AB}}$	$\frac{\text{Momentum diffusivity}}{\text{Solutal diffusivity}}$	$10 - 10^2$	$10^2 - 10^3$
Solutal Peclet No.	$Pe_c = ReSc \equiv \frac{VL}{\mathcal{D}_{AB}}$	$\frac{\text{Convective mass transport}}{\text{Diffusive mass transport}}$	$10^5 - 10^7$	$10^5 - 10^7$

Table 2. Order-of-magnitude estimates for dimensionless groups which characterize the CZ process.

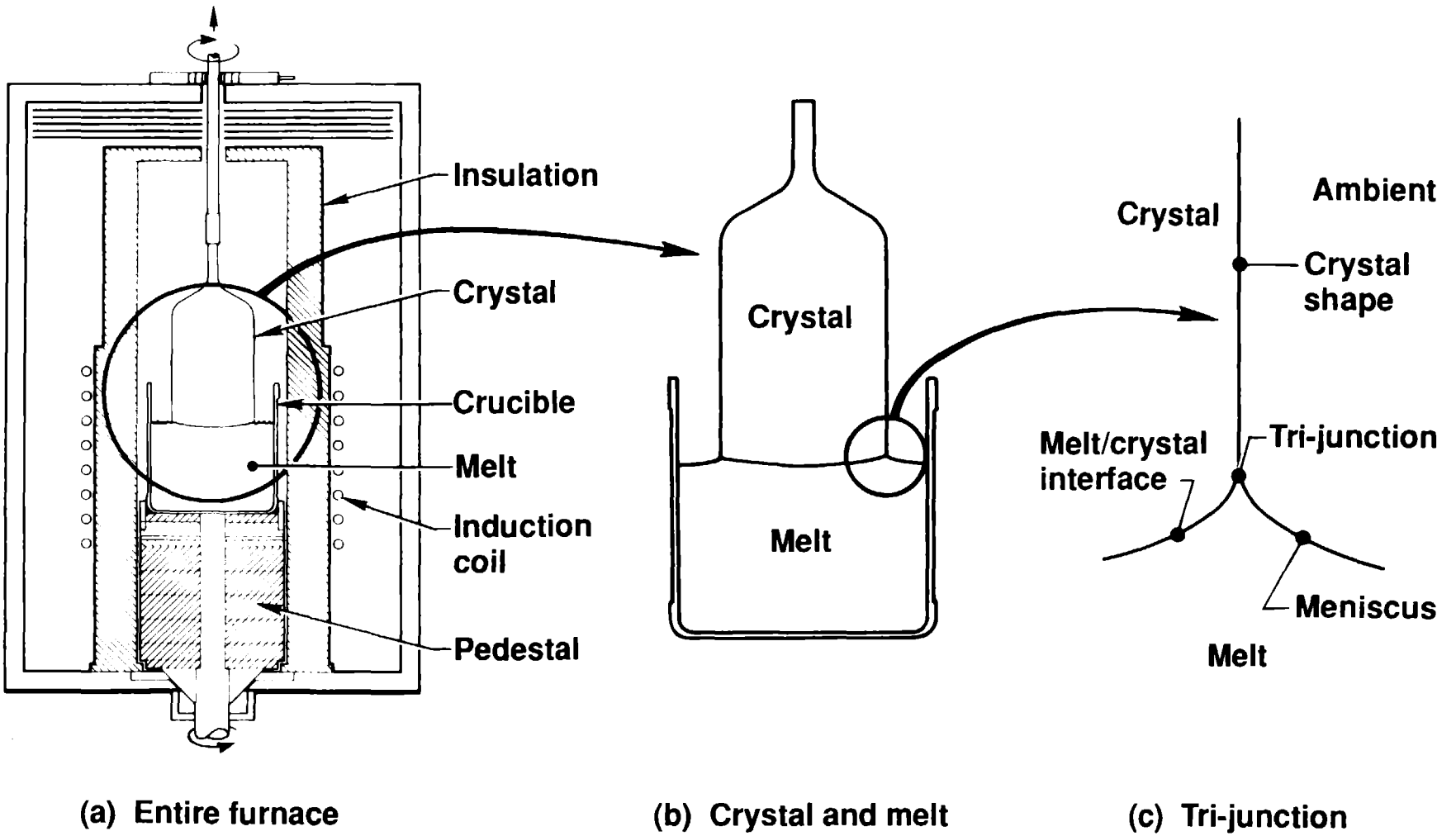

Figure 1. Schematic diagram of the Czochralski growth of an oxide crystal showing relevant length scales.

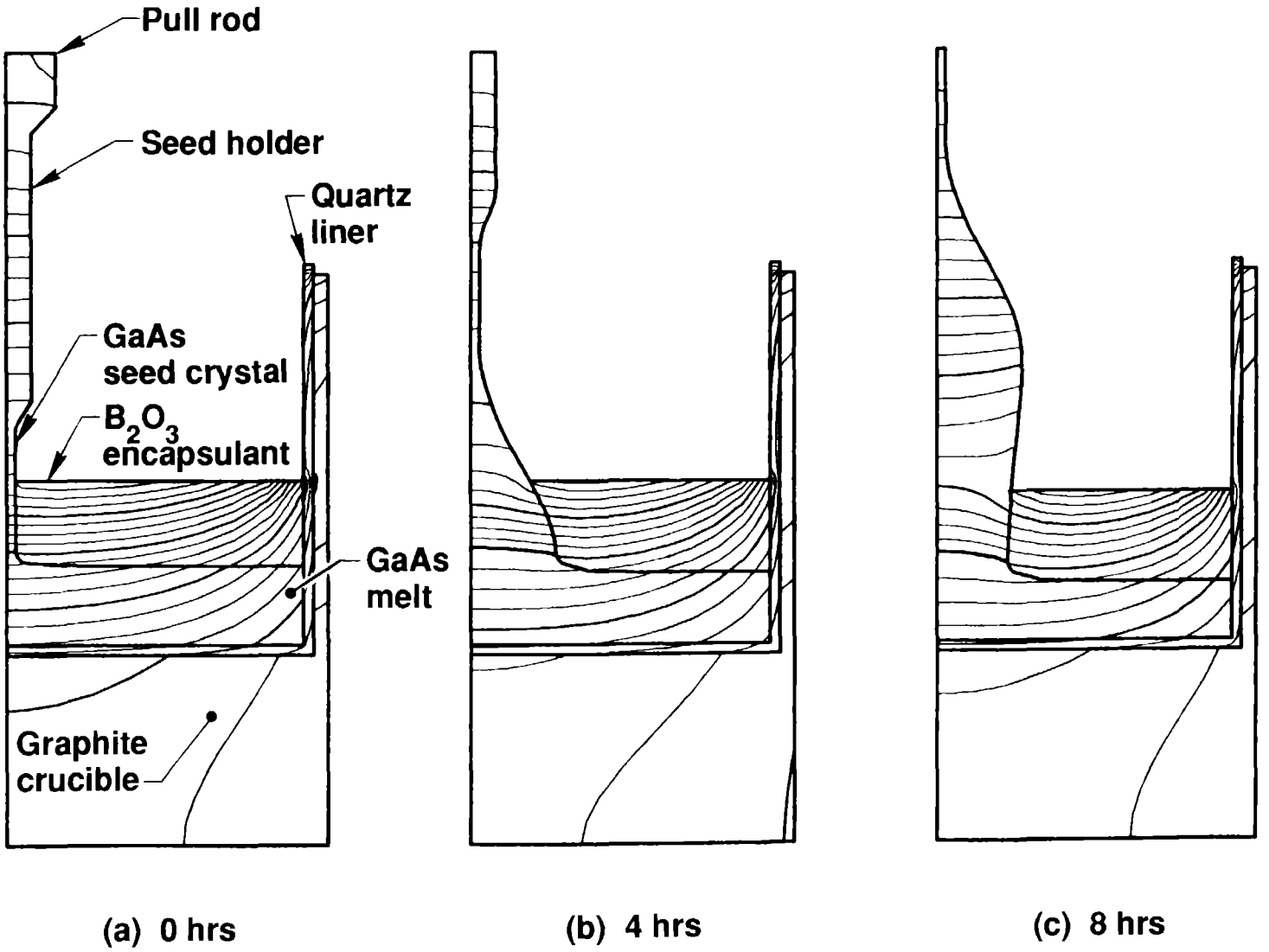

Figure 2. Results from the dynamic thermal-capillary model predicting the LEC growth of gallium arsenide, from [17].

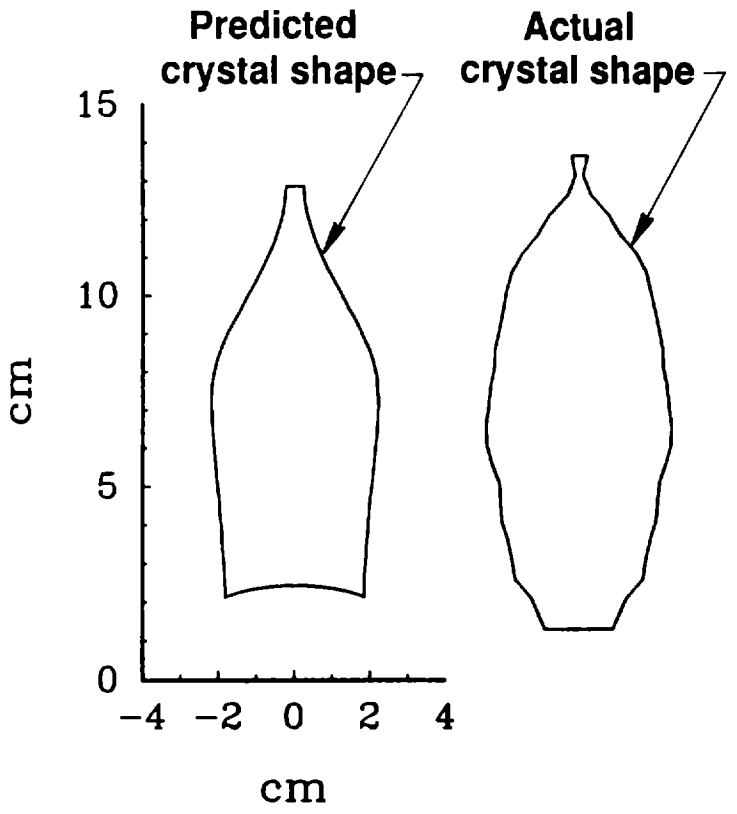

Figure 3. Comparison of theoretical and experimental GaAs crystal shapes, from [17].

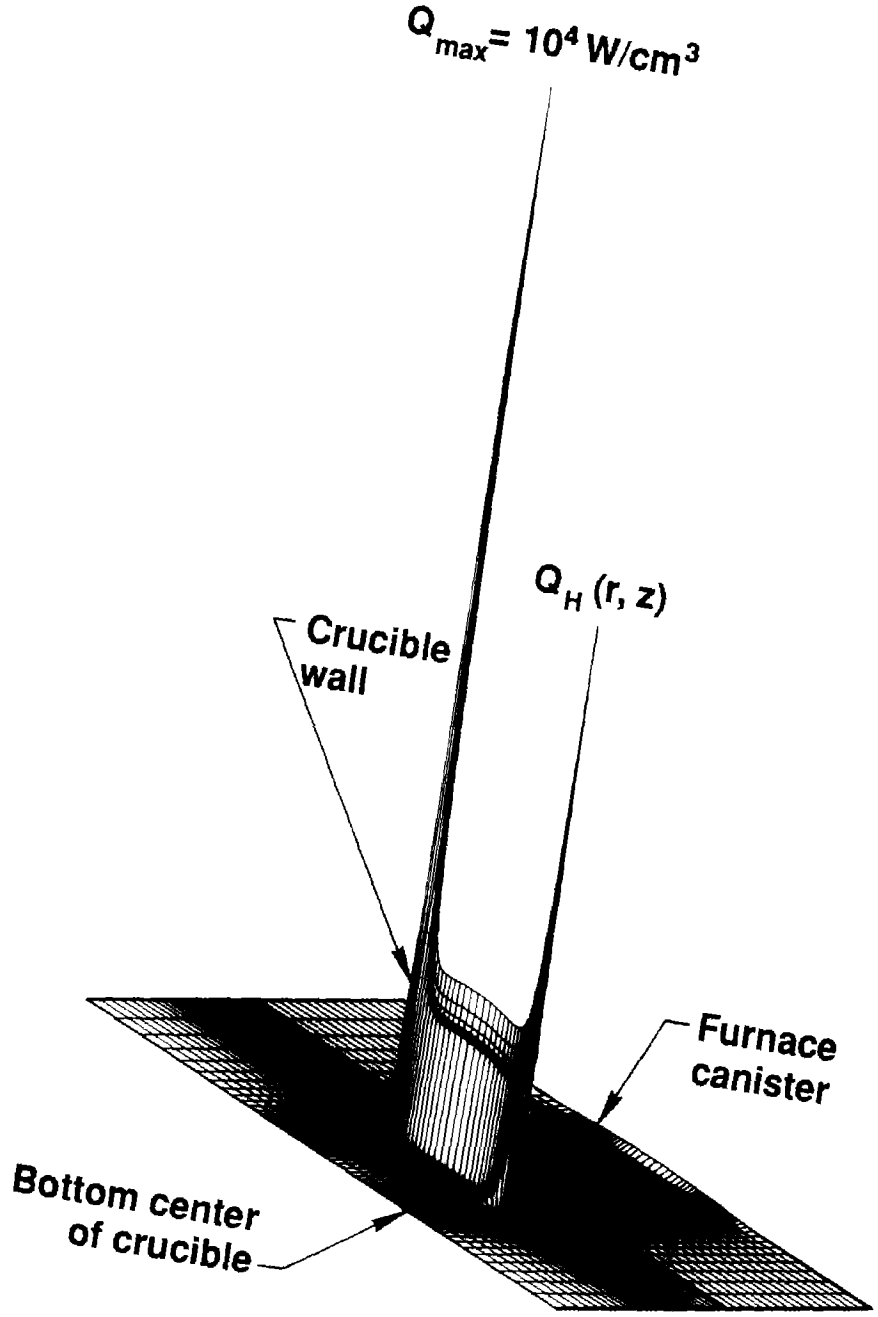

Figure 4. Induction power distribution delivered to iridium crucible, from [19]

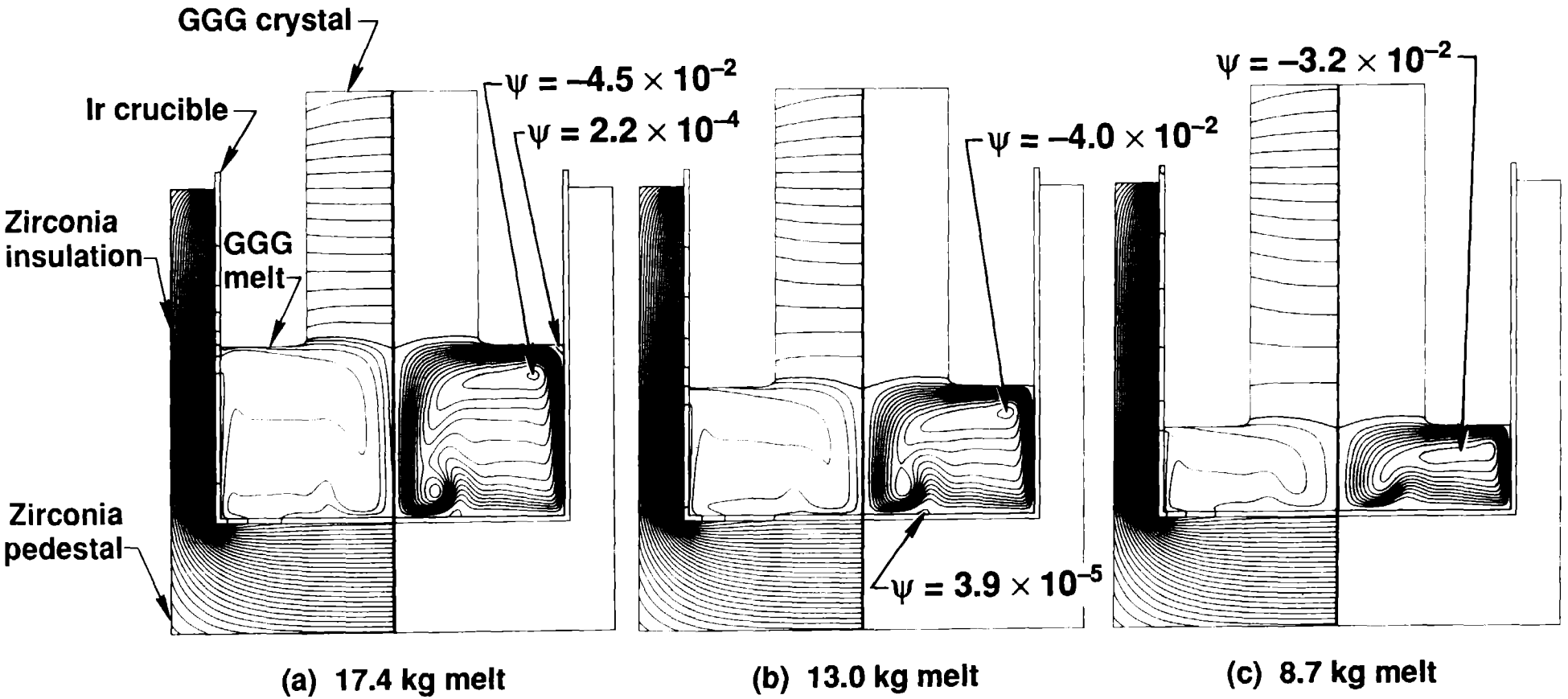

Figure 5. Quasi-steady-state simulation of GGG growth run, from [19]. Weights refer to amount of melt left in crucible.